AIP Journal of Applied Physics

Formation mechanisms of spatially-directed zincblende gallium nitride nanocrystals

A. W. Wood, R. R. Collino, B. L. Cardozo, F. Naab, Y. Q. Wang et al.

Citation: J. Appl. Phys. 110, 124307 (2011); doi: 10.1063/1.3665122
View online: http://dx.doi.org/10.1063/1.3665122
View Table of Contents: http://jap.aip.org/resource/1/JAPIAU/v110/i12
Published by the AIP Publishing LLC.

Additional information on J. Appl. Phys.

Journal Homepage: http://jap.aip.org/
Journal Information: http://jap.aip.org/about/about_the_journal
Top downloads: http://jap.aip.org/features/most_downloaded
Information for Authors: http://jap.aip.org/authors

ADVERTISEMENT

Downloaded 28 Jun 2013 to 141.211.173.82. This article is copyrighted as indicated in the abstract. Reuse of AIP content is subject to the terms at: http://jap.aip.org/about/rights_and_permissions

JOURNAL OF APPLIED PHYSICS **110**, 124307 (2011)

Formation mechanisms of spatially-directed zincblende gallium nitride nanocrystals

A. W. Wood,[1] R. R. Collino,[2,a)] B. L. Cardozo,[3] F. Naab,[4] Y. Q. Wang,[5] and R. S. Goldman[1,3,b)]

[1]*Department of Physics, University of Michigan, Ann Arbor, Michigan 48109, USA*
[2]*Department of Mechanical Engineering, University of Michigan, Ann Arbor, Michigan 48109, USA*
[3]*Department of Materials Science and Engineering, University of Michigan, Ann Arbor, Michigan 48109, USA*
[4]*Department of Nuclear Engineering and Radiological Sciences, University of Michigan, Ann Arbor, Michigan 48109, USA*
[5]*Materials Science and Technology Division, Los Alamos National Lab, Los Alamos, New Mexico 87545, USA*

(Received 11 August 2011; accepted 23 October 2011; published online 20 December 2011)

We report on the spatially selective formation of GaN nanocrystals embedded in GaAs. Broad-area N^+ implantation followed by rapid thermal annealing leads to the formation of nanocrystals at the depth of maximum ion damage. With additional irradiation using a Ga^+ focused ion beam, selective lateral positioning of the nanocrystals within the GaAs matrix is observed in isolated regions of increased vacancy concentration. Following rapid thermal annealing, the formation of zincblende GaN is observed in the regions of highest vacancy concentration. The nucleation of zincblende nanocrystals over the wurtzite phase of bulk GaN is consistent with the predictions of a thermodynamic model for the nanoscale size-dependence of GaN nucleation. © *2011 American Institute of Physics*. [doi:10.1063/1.3665122]

I. INTRODUCTION

Due to its direct energy gap in the visible wavelength range, GaN is suitable for use in visible light-emitters, diode lasers, and optical communications. While GaN usually crystallizes in a wurtzite (WZ) lattice, zincblende (ZB) GaN has also been reported, offering several advantages over WZ GaN including lower bandgaps ($3.28 - 3.23$ eV vs. 3.5 eV) (Refs. 1 and 2), and higher carrier mobilities.[3] In addition, ZB GaN may be readily integrated with existing ZB III-V semiconductor substrates and devices.[4] However, light-emitting diodes fabricated on $(1\ 0\ \bar{1}\ 0)$ *m* plane WZ GaN have shown polarized spontaneous light emission, potentially useful in liquid crystal display applications.[5] In addition, the piezoelectric WZ nitrides have potential applications in field-effect transistors tuned by applying stress to the device.[6] Ion beam synthesis approaches have been utilized to produce both ZB and WZ nitride nanocrystals.[7,8] The preference for ZB vs. WZ GaN may be related to nanocrystallite strain,[9] the relative stability of the small size of WZ and ZB nanocrystals,[10] or the influence of short-to-medium range order in the host matrix. To exploit the desired characteristics of both ZB and WZ GaN, an understanding of the mechanisms for selective phase nucleation is essential.

In terms of lateral patterning of nanocrystals, focused ion beam (FIB) milling has been used to produce sites for selective nucleation of Ge islands on Si(001),[11] Cu_2O nanodots on $SrTiO_3(100)$,[12] and InP nanowires on GaAs(100).[13] In addition, it has been proposed that FIB-induced vacancy motion would enable void organization in broad-area implanted GaSb and InSb.[14] In this paper, we report on the influence of combined broad-area and FIB irradiation, followed by rapid thermal annealing (RTA), on the phase selection and lateral patterning of nitride nanocrystals embedded in GaAs. Following N^+ implantation plus RTA, ZB GaN nanocrystals are observed to be centered about the depth of maximum ion damage. Additional Ga^+ FIB irradiation leads to selective lateral positioning of the nanocrystals in localized regions of highest vacancy concentration. The preferential nucleation of ZB GaN nanocrystals over the thermodynamically favored WZ phase of bulk GaN is consistent with the predictions of a thermodynamic model for the size-dependence of nucleation for ZB GaN.

This article is organized as follows: in Sec. II, we describe the methods used for synthesizing and characterizing the GaAs:N nanostructures, including ion implantation, transmission electron microscopy (TEM), and selected area electron diffraction (SAD). In Sec. III, we present damage-depth distributions for N^+ implantation into GaAs. We then examine the influence of localized damage on the lateral positioning of nanocrystal nucleation and propose a thermodynamic model for the nucleation of ZB GaN. A summary is given in Sec. IV.

II. EXPERIMENTAL PROCEDURES

For these investigations, $\sim$1 μm-thick *n*-doped GaAs films grown by molecular-beam epitaxy on (001) GaAs were broad-area implanted using 75 or 100 keV N^+ ions, with a nominal fluence of 2.5×10^{17} or 5×10^{17} cm^{-2}, respectively. To minimize channeling effects during implantation, a 7° angle of incidence with respect to the sample surface normal was used. During the broad-area N^+ implantation, the substrate temperature was maintained at 300 °C. Following

a)Present address: Department of Mechanical Engineering, University of California, Santa Barbara, Santa Barbara, CA 93106, USA
b)Author to whom correspondence should be addressed. Electronic mail: rsgold@umich.edu.

 © 2011 American Institute of Physics

Downloaded 28 Jun 2013 to 141.211.173.82. This article is copyrighted as indicated in the abstract. Reuse of AIP content is subject to the terms at: http://jap.aip.org/about/rights_and_permissions

broad-area implantation, trenches with widths and depths of 25 to 50 nm and spacings of 150 to 200 nm were milled into the surface using a Ga^+ FIB operating at 30 kV. The samples were then rapid thermal annealed in argon gas at 800 °C for 30 s. Cross-sectional TEM samples, oriented perpendicular to the length of the FIB-milled trenches, were prepared using FIB liftout.[15] TEM imaging and SAD were carried out in a JEOL 2010F TEM operating at 200 kV, using apertures which select regions with ~0.10 μm diameters. All SAD patterns were calibrated to the GaAs substrate {110}. SRIM (Ref. 16) simulations of vacancy and ion depth distribution were performed for 75 and 100 keV N^+ ions implanted into GaAs at a 7° angle of incidence. The depth-dependence of lattice disorder was determined by channeling-Rutherford backscattering spectrometry (RBS) with a 2 MeV He^{++} beam.

III. RESULTS AND DISCUSSION

A. Depth-dependence of ion damage

We first consider the influence of vacancy concentration on the depth distribution of nitride nanocrystal formation in GaAs. Figures 1(a) and 1(b) present dark-field TEM images of typical layers formed by 75 and 100 keV implantation-and-RTA. Figures 1(a) and 1(b) also contain overlaid plots of depth versus vacancy concentration and N concentration, as predicted by SRIM. The cavities in the TEM images, labeled with arrows, are likely remnants of coalesced N gas bubbles at the depths of highest N concentration, similar to earlier reports.[17,18] Simulations of 75 keV (100 keV) N^+ implantation predict maximum vacancy and N concentrations at depths of 100 (150) and 160 (200) nm, respectively. For 100 keV as-implanted GaAs, the maximum vacancy concentration is $\sim 1.9 \times 10^{25}$ cm^{-3}, compared to $\sim 1.0 \times 10^{25}$ cm^{-3} for the case of 75 keV as-implanted GaAs. In both cases, a surface layer containing a high density of GaN-rich GaAsN nanostructures within an amorphous matrix, centered about the predicted depth of maximum vacancy concentration, is observed. This suggests that lattice damage provides sites for nanocrystal nucleation.

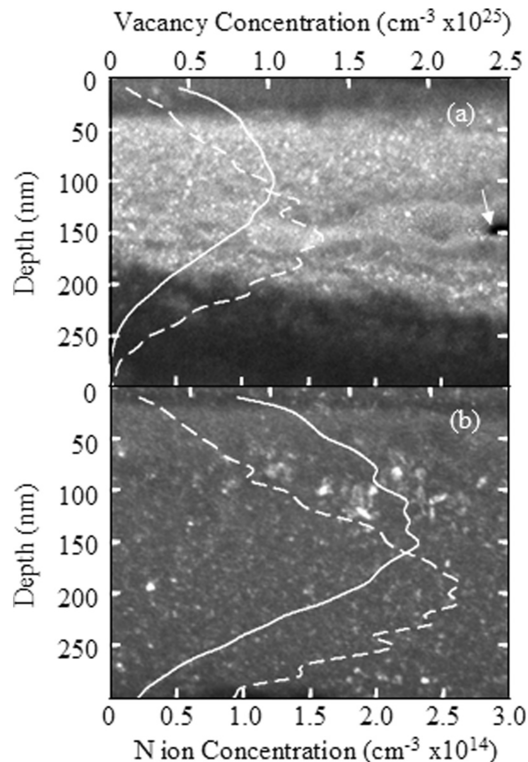

FIG. 1. SRIM simulations of the depth-dependence of vacancy and nitrogen concentrations for (a) 75 keV and (b) 100 keV N^+ ions implanted into GaAs, overlaid onto dark-field TEM images of implanted-and-RTA GaAs. The regions of highest vacancy concentration (solid line) and highest nitrogen concentration (dashed line) from the simulation correspond to layers with crystallite formation (bright spots) and blistering (arrows), as shown in the underlying images.

To determine the influence of broad-area N^+ implantation energy and RTA on damage depth profiles, (001) channeling-RBS measurements were performed on 75 and 100 keV N^+ implanted GaAs. Figure 2 presents the normalized yield versus energy and depth for 75 and 100 keV as-implanted and implanted-and-RTA GaAs. For comparison, random and (001) channeling yields from GaAs are included in the plot. The ratio of the channeling RBS yield to the random yield (χ) is a measure of the fraction of ions which were dechanneled, presumably due to lattice disorder. For 100 keV (75 keV) as-implanted GaAs, the normalized yield contains a broad peak spanning depths from 0 to 300 nm (0 to 250 nm). The presence of this peak indicates an increase in lattice disorder which encompasses both the depths of highest vacancy concentration and highest nitrogen concentration. For depths to 300 nm, the normalized yield is an average of 32% higher for 100 keV in comparison with that of 75 keV as-implanted GaAs, suggesting a higher vacancy concentration following 100 keV implantation, consistent with the predictions of SRIM simulations discussed above. Following RTA, the normalized yields of both the 100 keV and 75 keV samples are reduced, indicating partial recovery of crystallinity. For the 100 keV (75 keV) sample, the normalized yield contains a local minimum from 0 to 150 nm (0 to 100 nm), consistent with the predicted depth of maximum vacancy concentration and the observed depth of nanocrystal formation. Therefore,

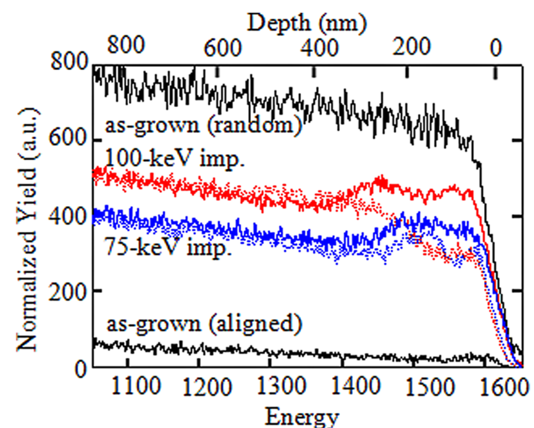

FIG. 2. (Color online) Channeling-RBS spectra consisting of the normalized yield of backscattered ions as a function of backscattered energy of GaAs layers. Data from 100 and 75 keV as-implanted (solid lines) and implanted-and-RTA (dashed lines) samples with GaAs in the random and (001) aligned configurations are compared. For the 75 keV (100 keV) as-implanted layer, a broad peak which spans depths from 0 to 250 nm (0 to 300 nm) is observed and attributed to an increase in lattice disorder. Following RTA, minima from 0 to 100 nm (0 to 150 nm) indicate partial recovery of the lattice damage, at depths corresponding to those where nanocrystal nucleation is observed.

Downloaded 28 Jun 2013 to 141.211.173.82. This article is copyrighted as indicated in the abstract. Reuse of AIP content is subject to the terms at: http://jap.aip.org/about/rights_and_permissions

the nanocrystal formation indeed takes place at the depth of highest vacancy concentration.

B. Nanoscale structure

We also consider the nanoscale structure following broad-area implantation, FIB processing to introduce regions of increased vacancy concentration, and RTA. Figure 3 presents typical dark-field diffraction contrast TEM images following (a) 75 keV implanted-plus-FIB-and-RTA and (c) 100 keV implanted-plus-FIB-and-RTA. Both TEM images reveal a series of hills and valleys associated with the FIB-milled trenches, along with two distinct regions below the Pt layer: (1) a nanocrystal bilayer with a ~20 nm thick surface layer and a 250 nm thick nanocrystal middle layer, and (2) a near-substrate layer.

We compare the nanoscale structure for both implantation energies. The formation of nanocrystals within the bilayer is comparable to the nanocrystal layer formed via matrix-seeded growth;[7] within the nanocrystal bilayer of the implanted-plus-FIB-and-RTA samples, the thickest layer contains nanocrystals in an amorphous matrix. The nanocrystals have an average radius of 1.04 ± 0.53 (75 keV) and 1.37 ± 0.36 (100 keV) nm. In addition, within the narrowest layer of the bilayer, it appears that many ~10–15 nm nanocrystallite clusters have formed within a ~20 nm amorphous layer at the surface. The thickness of the amorphous layer is consistent with SRIM simulations of the depth of highest vacancy concentration introduced by 30 keV Ga^+ FIB irradiation. The nanocrystallite clusters have nucleated near the FIB-irradiated trenches, suggesting a preference for nucleation in regions of increased vacancy concentration.

For both broad-area implantation energies, we consider the influence of FIB irradiation on the percentage of preferentially aligned nanocrystals within the nanostructured bilayer. In the vicinity of the FIB-irradiated regions, similar densities of nanocrystallite clusters are apparent following implantation-plus-FIB-and-RTA at both implantation energies. However, a comparison of the FIB-irradiated regions reveals

TABLE I. A comparison of the interplanar distances determined by selected area diffraction of GaAs:N following RTA at 550 and 600 °C with the powder diffraction data for GaAs and GaN.

d-spacing (Å) (experimental)		Powder diffraction standards (Å)	
75-keV implant.	100-kev implant.	ZB GaN (hkl)	GaAs (hkl)
3.26	3.26		3.26 (111)
2.56	2.59	2.60 (111)	
2.00	2.00		2.00 (220)
1.71	1.71		1.70 (311)
	1.62	1.59 (220)	
1.41	1.39		1.41 (400)
1.30	1.31		1.30 (331)

a lower density of randomly spaced nanocrystals in the 75 keV bilayer, due to a lower vacancy concentration. The vacancy concentrations for the 75 and 100 keV as-implanted GaAs are shown in Figs. 1(a) and 1(b), respectively. Since the 75 keV implantation leads to ~50% fewer vacancies in comparison to that of the 100 keV implantation, there are fewer available nucleation sites in that case. Thus, subsequent FIB irradiation is expected to provide the greatest selectivity for the 75 keV implanted-plus-FIB-and-RTA films.

Identification of nanocrystals was performed using SAD collected from the bilayer following 75 keV and 100 keV implantation-plus-FIB-and-RTA, as shown in Figs. 3(b) and 3(d), respectively. Both SAD patterns contain several spotty rings associated with the nanocrystals and a diffuse ring, presumably due to the amorphous regions. Comparisons of the interplanar spacings determined by SAD and the powder diffraction standards from GaAs and GaN are shown in Table I. For the 75 keV (100 keV) implanted-plus-FIB-and-RTA nanocrystal bilayer, d-spacings of 3.26, 2.00, 1.71, 1.41 and 1.30 Å (3.26, 2.00, 1.71, 1.39, and 1.31 Å) are observed, within 1.4% of the {111}, {220}, {311}, {400}, and {331} interplanar spacings of GaAs. Additionally, for the 75 keV (100 keV) implanted-plus-FIB-and-RTA nanocrystal bilayer, d-spacings of 2.56 Å (2.59 and 1.62 Å) are apparent, within 1.9% of the {111} ({111} and {220}) interplanar spacings

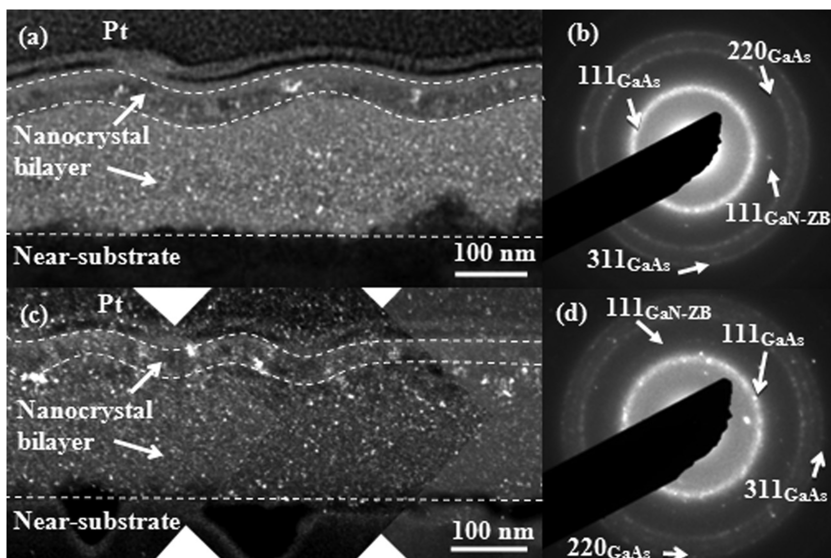

FIG. 3. Dark field TEM image of (a) 75 keV and (c) 100 keV implanted-plus-FIB-and-RTA GaAs. Polycrystalline nanocrystals with a clustering of crystallites near the bottom of the FIB milled trenches appear as bright spots in the TEM image. The SAD patterns collected from the polycrystalline layers of (a) and (c), shown in (b) and (d), reveal the formation of ZB GaN in both cases.

Downloaded 28 Jun 2013 to 141.211.173.82. This article is copyrighted as indicated in the abstract. Reuse of AIP content is subject to the terms at: http://jap.aip.org/about/rights_and_permissions

of ZB GaN. The {220} reflection of ZB GaN is likely missing for the 75 keV case due to the low density of GaN nanocrystals. As shown in Fig. 1, there are fewer vacancies expected following 75 keV implantation in comparison with that of 100 keV implantation, which results in fewer nanocrystal nucleation sites. For both implantation energies, preferential nucleation of ZB GaN is indicated by the presence of the {111} reflections of ZB GaN, while the {110} reflections of WZ GaN are absent. It is interesting to note that the ZB phase has formed following both 75 and 100 keV implantation-plus-FIB-and-RTA, although WZ is predicted to be the most stable thermodynamically.[19]

C. Mechanisms for ZB GaN nucleation

The proposed nanocrystal nucleation process following broad-area implantation, FIB processing, and RTA is shown schematically in Fig. 4. The implantation of GaAs with high energy N^+ ions produces a N super-saturated surface layer, as shown in Fig. 4(a). The subsequent surface exposure to localized FIB irradiation introduces regions of increased vacancy concentration which act as nanocrystal nucleation sites

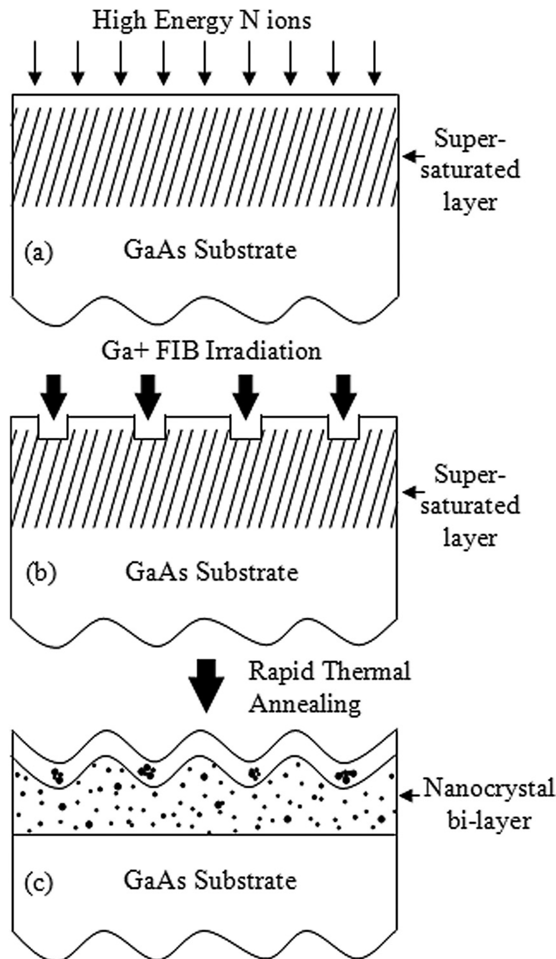

FIG. 4. Schematic of the directed matrix seeding process, consisting of (a) broad-area high energy nitrogen ion irradiation to produce a N super-saturated amorphous layer, (b) FIB irradiation to produce arrays of localized high vacancy concentration, and (c) rapid thermal annealing to enable spatially–directed nanocrystal nucleation.

(Fig. 4(b)). Following annealing, a nanostructured bilayer is formed at the surface, as shown in Fig. 4(c).

We examine the size-dependence of nanocrystal phase by considering the free energy for the nucleation of ZB and WZ GaN. The nanocrystals form in an amorphous matrix; thus, strain is not expected to play a role in their nucleation. Therefore, we assume an unstrained spherical solid nucleating from a liquid. We note that the change in free energy needed for the formation of a solid nucleus with volume V_s and surface area A_{sL} is given by

$$\Delta G = V_s\left(\frac{G_v^s}{V_m} - \frac{G_v^L}{V_m}\right) + A_{sL}\gamma_{sL}, \tag{1}$$

where G_v^s and G_v^L are the Gibbs free energy of the solid and liquid, respectively; γ_{sL} is the interface energy between the cluster and the surrounding matrix; and V_m is the molar volume.

We now consider the term $G_v^s - G_v^L$. At a temperature, T, the change in free energy is

$$G_v^s - G_v^L = \Delta H_v - T\Delta S_v. \tag{2}$$

$G_v^s - G_v^L$ must be less than 0 for energetically favorable solidification. Let T_n be the temperature at which nucleation occurs. Then

$$\Delta H_v(T_n) - T_n\Delta S_v = 0, \tag{3}$$

$$\Delta S_v = \frac{\Delta H_v(T_n)}{T_n}. \tag{4}$$

In the temperature range of 298 to 1400 K, the formation enthalpy of GaN fluctuates by $\sim$5%;[20] therefore, we consider it to be temperature-independent. Inserting Eq. (4) into Eq. (2), we obtain

$$G_v^s - G_v^L = \Delta H_v - T\frac{\Delta H_v}{T_n}. \tag{5}$$

Substituting Eq. (5) into Eq. (1), we obtain the following expression for the change in free energy:

$$\Delta G = V_s\left(\frac{\Delta H_v}{V_m} - T\frac{\Delta H_v}{V_m T_n}\right) + A_{sL}\gamma_{sL}. \tag{6}$$

To calculate the interfacial energy, we consider the method of Miedema and den Broeder.[21] We approximate the crystal-melt interface entropy to be that of Ga and obtain the following expression for the interface energy between the solid GaN cluster and the liquid matrix:

$$\gamma = 2.5E - 9\frac{\Delta H_v}{V_m^{2/3}} + 0.65E - 10\frac{\mathrm{T}_n}{V_m^{2/3}} \tag{7}$$

with energy units of kJ.

To calculate the total free energy, we consider the enthalpy of formation of ZB and WZ GaN. For WZ GaN, we

Downloaded 28 Jun 2013 to 141.211.173.82. This article is copyrighted as indicated in the abstract. Reuse of AIP content is subject to the terms at: http://jap.aip.org/about/rights_and_permissions

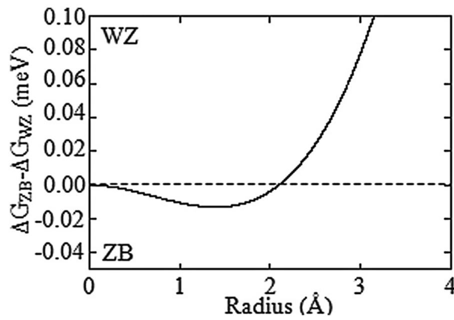

FIG. 5. Plot of the difference between the free energies of formation for WZ and ZB GaN following RTA at 800 °C. For radii less than 2.10 Å, the ZB phase is thermodynamically favored, while the WZ phase is favored for larger radii.

use $\Delta H_v^{WZ} = -131.326\,\mathrm{kJ/mol}$.[20] We consider the relative enthalpies of GaN at low pressures, with $\Delta H_v^{ZB} = 0.991\,\Delta H_v^{WZ}$.[22] We therefore use a value of $\Delta H_v^{ZB} = -130.144$ kJ/mol. For RTA at 800 °C, the change in free energy as a function of radius for ZB and WZ GaN becomes

$$\Delta G^{ZB} = r^3(-2.833E - 23\mathrm{kJ}/A^3) + r^2(8.588E - 23\mathrm{kJ}/A^2) \tag{8}$$

$$\Delta G^{WZ} = r^3(-2.987E - 23\mathrm{kJ}/A^3) + r^2(8.911E - 23\mathrm{kJ}/A^2). \tag{9}$$

The resulting difference in free energies, $\Delta G_{ZB} - \Delta G_{WZ}$, as a function of nanocrystal radius, is shown in Fig. 5. For implantation-plus-RTA, ZB GaN is favored when $r < 2.10$ Å. For small r, the reduction in free energy of the ZB phase in comparison with the WZ is driven by a minimization of the GaN surface energy. Indeed, the surface energy is minimized by adoption of the ZB crystal structure, which has a higher density of low energy {111} surface planes in comparison with the WZ structure. We note that a more accurate prediction of the size-dependence of WZ vs. ZB nanocrystal formation is expected once the enthalpy and interfacial energies of nanoscale GaN are available.

IV. CONCLUSIONS

In summary, we have examined the formation of nitride nanocrystals using a combination of broad-area implantation and FIB processing. GaN nanocrystals form in the regions of highest damage, both vertically and laterally. Thus, lateral positioning using FIB patterning to introduce localized regions of vacancy concentration is possible. Following RTA, ZB GaN nanocrystals have nucleated instead of the thermodynamically favored WZ phase of bulk GaN. Nucleation of ZB nanocrystals is consistent with the predictions of a thermodynamic model for nucleation of nano-scale ZB GaN.

ACKNOWLEDGMENTS

This work was supported in part by the U.S. Department of Defense through the Intelligence Community Postdoctoral Research Fellowship under grant HM1582-05-1-2027, by the AFOSR through the MURI program under Grant No. FA9950-08-1-0340, the CIA under Contract No. 2007-0919714-000, and by NSF under Grant No. CMMI 0700301. Support for Y. Q. W. was provided by the Center for Integrated Nanotechnologies jointly operated by Los Alamos and Sandia National Laboratories.

[1]G. Ramírez-Flores, H. Navarro-Contreras, A. Lastras-Martínez, R. C. Powell, and J. E. Greene, Phys. Rev. B **50**, 8433 (1994).
[2]Z. Sitar, M. J. Paisley, J. Ruan, J. W. Choyke, and R. F. Davis, J. Mater. Sci. Lett. **11**, 261 (1992).
[3]P. Das and D. K. Ferry, Solid-State Electron. **19**, 851 (1976).
[4]B. Monemar, J. Mater. Sci.: Mater. Electron. **10**, 227 (1999).
[5]N. F. Gardner, J. C. Kim, J. J. Wierer, Y. C. Shen, and M. R. Krames, Appl. Phys. Lett. **86**, 111101 (2005).
[6]Z. L. Wang, Adv. Mater. **19**, 889 (2007).
[7]X. Weng, S. J. Clarke, W. Ye, S. Kumar, R. S. Goldman, A. Daniel, R. Clarke, J. Holt, J. Sipowska, A. Francis, and V. Rotberg, J. Appl. Phys. **92**, 4012 (2002).
[8]X. W. Lin, M. Behar, R. Maltez, W. Swider, Z. Liliental-Weber, and J. Washburn, Appl. Phys. Lett. **67**, 2699 (1995).
[9]T. Ito, K. Shiraishi, and A. Taguchi, J. Cryst. Growth **227–228**, 366 (2001).
[10]R. Banerjee, R. Jayakrishnan, and P. Ayyub, J. Phys. Condens. Matter **12**, 10647 (2000).
[11]M. Kammler, R. Hull, M. C. Reuter, and F. M. Ross, Appl. Phys. Lett. **82**, 1093 (2003).
[12]J. F. Groves, Y. Du, I. Lyubinetsky, and D. R. Baer, Superlattices Microstruct. **44**, 677 (2008).
[13]J. Ahopelto, H. Lezec, Y. Ochiai, A. Usui, and H. Sakaki, Appl. Phys. Lett. **64**, 499 (1994).
[14]N. Nitta and M. Taniwaki, Nucl. Instrum. Methods Phys. Res. B **206**, 482 (2003).
[15]L. A. Giannuzzi, J. L. Drown, S. R. Brown, R. B. Irwin, and F. A. Stevie, Microsc. Res. Tech. **41**, 285 (1998).
[16]J. F. Ziegler, J. P. Biersack, and U. Littmark, *The Stopping Range of Ions in Matter* (Pergamon, New York, 1985).
[17]R. R. Collino, B. B. Dick, F. Naab, Y. Q. Wang, M. D. Thouless, and R. S. Goldman, Appl. Phys. Lett. **95**, 111912 (2009).
[18]X. Weng, W. Ye, J. C. Mabon, and R. S. Goldman, J. Vac. Sci. Technol. B **22**, 989 (2004).
[19]M. Leszczynski, in *Properties, Processing and Applications of Gallium Nitride and Related Semiconductors*, edited by J.H. Edgar, S.T. Strite, I. Akasaki, H. Amano, and C. Wetzel (INSPEC, London, United Kingdom, 1999), p. 3.
[20]K. T. Jacob, and G. Rajitha, J. Cryst. Growth **311**, 3806 (2009).
[21]A. R. Miedema and F. J. A. den Broeder, Z. Metallkd **70**, 14 (1979).
[22]X. Sun, Q. Chen, Y. Chu, and C. Wang, Physica B **368**, 243 (2005).

Downloaded 28 Jun 2013 to 141.211.173.82. This article is copyrighted as indicated in the abstract. Reuse of AIP content is subject to the terms at: http://jap.aip.org/about/rights_and_permissions